ADVANCES IN ATMOSPHERIC SCIENCES, VOL. 36, APRIL 2019, 346–362

• **Original Paper** •

Seasonal Variations of Observed Raindrop Size Distribution in East China

Long WEN[1,2,3], Kun ZHAO*[1,2], Mengyao WANG[1], and Guifu ZHANG[1,4]

[1]*Key Laboratory of Mesoscale Severe Weather of Ministry of Education and School of Atmospheric Sciences,*
Nanjing University, 163 *Xianlin Road, Nanjing* 210023*, China*
[2]*State Key Laboratory of Severe Weather and Joint Center for Atmospheric Radar Research of China Meteorological Administration and*
Nanjing University, Chinese Academy of Meteorological Sciences, Beijing 100081*, China*
[3]*Xichang Satellite Launch Center, Xichang* 615000*, China*
[4]*School of Meteorology and Center for Analysis and Prediction of Storms, University of Oklahoma, Norman Oklahoma* 73072*, USA*

(Received 8 May 2018; revised 12 November 2018; accepted 17 December 2018)

ABSTRACT

Seasonal variations of rainfall microphysics in East China are investigated using data from the observations of a two-dimensional video disdrometer and a vertically pointing micro rain radar. The precipitation and rain drop size distribution (DSD) characteristics are revealed for different rain types and seasons. Summer rainfall is dominated by convective rain, while during the other seasons the contribution of stratiform rain to rainfall amount is equal to or even larger than that of convective rain. The mean mass-weighted diameter versus the generalized intercept parameter pairs of convective rain are plotted roughly around the "maritime" cluster, indicating a maritime nature of convective precipitation throughout the year in East China. The localized rainfall estimators, i.e., rainfall kinetic energy–rain rate, shape–slope, and radar reflectivity–rain rate relations are further derived. DSD variability is believed to be a major source of diversity of the aforementioned derived estimators. These newly derived relations would certainly improve the accuracy of rainfall kinetic energy estimation, DSD retrieval, and quantitative precipitation estimation in this specific region.

Key words: raindrop size distribution, precipitation microphysics, disdrometer, seasonal variation, East China

Citation: Wen, L., K. Zhao, M. Y. Wang, and G. F. Zhang, 2019: Seasonal variations of observed raindrop size distribution in East China. *Adv. Atmos. Sci.*, **36**(4), 346–362, https://doi.org/10.1007/s00376-018-8107-5.

Article Highlights:

- Precipitation and raindrop size distribution characteristics in East China vary across seasons and rain types.
- Convective rain in East China exhibits a maritime nature with high concentration of small drops throughout the year.
- Empirical relations are derived to improve rainfall kinetic energy estimation, DSD retrieval, and quantitative precipitation estimation.

1. Introduction

Raindrop size distributions (DSDs) are an important characteristic of rainfall microphysical processes. By using observations from advanced instruments such as surface disdrometers and polarimetric radar, rain DSDs have been studied globally. In correspondence with different rain types and climatic locations, rain DSDs are known to vary both spatially and temporally around the world (e.g., Tokay and Short, 1996; Bringi et al., 2003; Chen et al., 2013; Wen et al., 2016). Knowledge of DSD variability is not only important for improving the accuracy of quantitative precipitation estimation (QPE) and model parameterization (Zhang et al., 2006), but also very useful in many application fields concerning microwave communication (Timothy et al., 2002), radar and satellite remote sensing (Vivekanandan et al., 2004; Krajewski et al., 2006; Liao et al., 2014; Chen et al., 2017b), and soil erosion (Salles et al., 2002; Meshesha et al., 2014; Carollo et al., 2016).

As variability in DSDs usually reflect the changes in microphysical processes of rain (Rosenfeld and Ulbrich, 2003), many studies have been carried out based on observations from midlatitude to tropical and equatorial zones (e.g., Zawadzki and De Agostinho Antonio, 1988; Kozu et al., 2005; Kumar et al., 2011; Janapati et al., 2017; Das and Maitra, 2018), and also from both maritime and continental environments (Tokay and Short, 1996; Bringi et al., 2003; Ulbrich and Atlas, 2007; Niu et al., 2010). Besides the abovementioned studies of DSD variations in different climatic regions,

---

* Corresponding author: Kun ZHAO
E-mail: zhaokun@nju.edu.cn

efforts have also been conducted to understand the variations of DSD in different rain types and events (Tokay and Short, 1996; Maki et al., 2001; Wen et al., 2016; Das et al., 2017), as well as on various time scales (e.g., Rao et al., 2009).

The variation in DSDs on different time scales (from diurnal to seasonal) has been studied in the Asian monsoon region—specifically, in India (e.g., Radhakrishna et al., 2009; Rao et al., 2009; Chakravarty and Raj, 2013; Chakravarty et al., 2013; Kumar and Reddy, 2013; Jayalakshmi and Reddy, 2014; Das and Ghosh, 2016) and the Southeast Asia region (e.g., Kozu et al., 2006; Ushiyama et al., 2009; Krishna et al., 2016; Seela et al., 2017). Rao et al. (2009) showed that the DSD over Gadanki (in the southeast Indian peninsular) varies significantly between different monsoonal seasons. Radhakrishna et al. (2009) found that the seasonal differences in DSD is a regular feature in Southeast India, and reported that the concentration of small drops in the northeast monsoon season is higher than that of the southwest monsoon season. Jayalakshmi and Reddy (2014) reached the same conclusion for rainfall in Kadapa, a semi-arid continental site in India. Further environmental analysis by Radhakrishna et al. (2009) revealed that the differences in evaporation and strong updrafts during different seasons plays an important role in the seasonal variability of DSDs. Chakravarty and Raj (2013) and Chakravarty et al. (2013) demonstrated that, due to the convective nature of rainfall, larger drops are more prevalent during pre- and post-monsoon months than in the monsoon season over two different sites in India. The variability of DSD and the resultant seasonal dependence of QPE estimators in Ahmedabad, India, were further evaluated by Das and Ghosh (2016).

Kozu et al. (2006) found that the difference in precipitation characteristics during different monsoon seasons results in large seasonal variation of DSDs in India, whereas Sumatra has the most significant diurnal variation of DSDs caused by local convection. Singapore is affected by both land and oceanic precipitation, and thus its rain DSDs show the less diurnal and seasonal variation. Subsequently, Ushiyama et al. (2009) reported that the amplitude of the seasonal DSD variation over Palau is approximately the same as that in Singapore and Sumatra. Larger mean drop diameters in the westerly monsoon season compared to the easterly monsoon season over Palau were investigated in Ushiyama et al. (2009) and Krishna et al. (2016). Further comparison of DSDs between Taiwan and Palau during summer season in Seela et al. (2017) showed significant differences. In Taiwan, terrain-influenced clouds extend to higher altitudes, resulting in a higher concentration of medium- and large-sized drops as compared to Palau.

The climate in East China is greatly influenced by the East Asian monsoon. The structure and main components of the East Asian monsoon are likely to be independent of the Indian monsoon system (Ding and Chan, 2005). As a result, rainfall in this region is usually characterized by unique precipitation microphysics that differ from those in India and Southeast Asia. Rain DSD characteristics in this region have been evaluated in previous works, but mainly based on case studies, e.g., for typhoons (Chen et al., 2012; Wang et al., 2016; Wen et al., 2018), squall lines (Jung et al., 2012; Chen et al., 2015; Wen et al., 2017b), and mei-yu precipitation (Shusse et al., 2011; Oue et al., 2015; Wen et al., 2015).

Latterly, the statistical DSD characteristics of three mei-yu seasons in East China were examined in Chen et al. (2013). Compared to Chen et al. (2013), Tang et al. (2014) further showed that the DSDs in North and South China during summer are generally characterized by a lower raindrop diameter than mei-yu precipitation in East China. Using 2-D video disdrometer (2DVD) and collocated micro rain radar (MRR) data, our previous study further helped demonstrate the statistical DSD characteristics in East China in summer (Wen et al., 2016). As demonstrated by Rosenfeld and Ulbrich (2003), the regional-scale DSD variation is mostly affected by the localized (maritime or continental) cloud microstructure. In Wen et al. (2016), we revealed that the summer convection in East China is more like “maritime” convection. The warm and moist air that is transported by the dominant southerly winds from the ocean to the continent of China during summer is believed to be the main cause.

More recently, the diurnal variation of DSDs over the central Tibetan Plateau in West China were revealed by Chen et al. (2017a), and a boarder spectrum of daytime convective DSDs was found, characterized by fewer (more) small (large) drops than the nighttime case. Furthermore, Wen et al. (2017a) analyzed the characteristics of summer rainfall and winter snowfall events over North China. In their study, summer convective rain oriented from a local region, north, and west was found to be continental, but that produced by a typhoon system was recognized as maritime-like convection. Besides these studies, however, to the best of our knowledge, the seasonal variations of DSDs have received limited investigation and remain unknown in China due to the lack of long-term DSD measurements by high-precision disdrometers.

In May 2014, a field campaign named “Observation, Prediction and Analysis of Severe Convection of China” (OPACC, Xue, 2016) was conducted in the Yangtze–Huaihe River Basin. A 2DVD and MRR were installed in Nanjing, Jiangsu Province, to observe the dynamical and microphysical characteristics of precipitation in this region (Wen et al., 2016; Wen et al., 2017c). Nanjing is located in East China, and is greatly influenced by the East Asian monsoon (Ding and Chan, 2005), making it a suitable location for the study of seasonal variations of DSDs. Until June 2016, two years of continuous 2DVD and MRR data were obtained with an in-situ tipping-bucket rain gauge (0.1 mm resolution). Using these unique datasets, the objective of this study is to better reveal the seasonal variations of DSDs in this specific region.

2. Data and methods

2.1. *Instruments and data*

In this study, the rainfall and disdrometer data were collected at Jiangning national weather station (JN; 31.93°N, 118.90°E), Nanjing, from 1 June 2014 to 31 May 2016. The

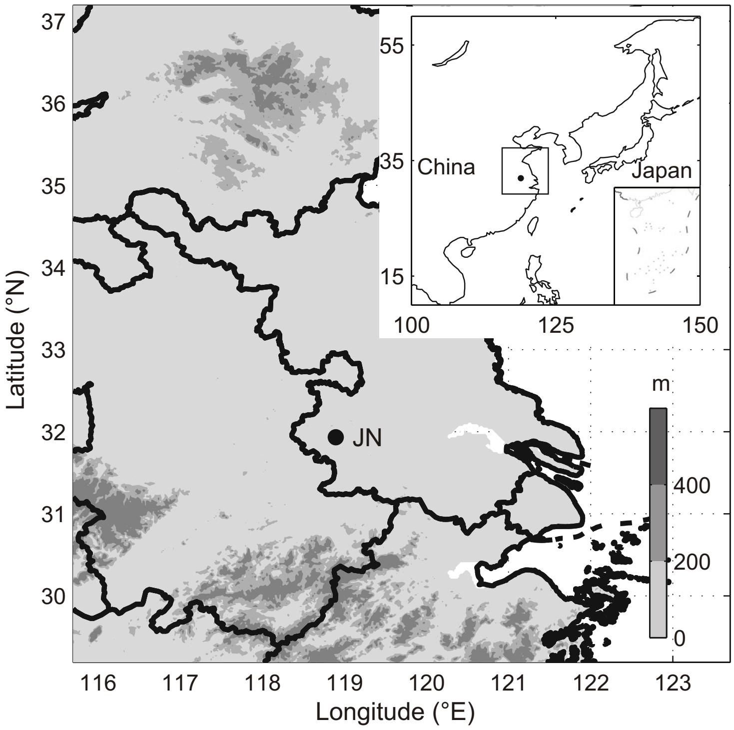

Fig. 1. Location of the site at Jiangning (JN), with shading representing the local topography around the JN site.

geographic location of the JN site is shown in Fig. 1. The MRR was located on the roof of a building at the JN site, approximately 20 m away from the 2DVD on the ground.

The third-generation 2DVD is designed to mitigate splashing and wind-induced errors. The range of raindrop diameter bins is 0.1–8.1 mm (sorted into a 0.2-mm resolution, i.e., 41 bins). The fall speed for each velocity bin is averaged from all of the drop velocities within the corresponding size bin. The MRR can observe 30 vertical levels (200-m resolution) in the atmosphere, and can also estimate DSDs by utilizing the empirical relationship between raindrop size and fall velocity (Peters et al., 2002). The fine precision of the MRR's precipitation and DSD measurements near the ground were evaluated through a comparative study with the collocated 2DVD in our previous works (Wen et al., 2015, 2017c). Note that the MRR data used here are only for the purpose of rain type classification. A more detailed description of the two instruments and the data processes can be found in our previous works (Wen et al., 2016, 2017c).

The temporal resolution for the 2DVD, MRR, and rain gauge data is 1 min in this study. The snowfall data in winter are excluded artificially according to the observation record from the JN site run by the China Meteorological Administration. Meanwhile, the velocity-based filter used in this study (see section 2.3) can also help to exclude the snowfall samples, because snowflakes fall much slower than raindrops at a similar size (Brandes et al., 2007). Moreover, the NCEP-II Reanalysis (R2) (Kanamitsu et al., 2002) data (2.5° × 2.5°, monthly) from June 2014 to May 2016 are used to elucidate the climatological background of different seasons in East China. Specifically, in this study, summer comprises the months of June, July, and August, autumn is September–October–November, winter is December–January–February, and spring is March–April–May.

2.2. *Gamma DSD model*

The widely accepted gamma model applied to rain DSDs (Ulbrich, 1983) is given as

$$N(D) = N_0 D^{\mu} e^{-\Lambda D} , \tag{1}$$

where D (mm) represents the equivolume diameter, and N_0 ($\mathrm{m}^{-3}\ \mathrm{mm}^{-1-\mu}$), μ (dimensionless), and Λ (mm^{-1}) are the three control parameters of the gamma model, named the intercept, the shape, and the slope parameters, respectively.

In this study, the three control parameters are derived from the gamma DSD using the M246 truncated moment fitting method (Vivekanandan et al., 2004). Other integral rainfall and DSD parameters of interest here, including the rain rate (R, mm h^{-1}), liquid water content (LWC, g m^{-3}), mass-weighted mean diameter (D_{m}, mm), generalized intercept parameter (N_{w}, $\mathrm{mm}^{-1}\ \mathrm{m}^{-3}$), radar reflectivity factor (Z, $\mathrm{mm}^6\ \mathrm{m}^{-3}$), and total concentration of raindrops (N_{t}, m^{-3}), are all computed from the nth-order weighted moment of the measured DSD directly. Detailed expressions for the above-mentioned computed parameters are all given in Wen et al. (2016).

2.3. *Fall velocity measurements from 2DVD*

Previous studies have indicated that 2DVD observations suffer from errors of oversampling small raindrops as well as the splash effect (e.g., Chang et al., 2009). To remove the super-terminal (splashing) drops, we applied the same particle-size-versus-fall-velocity filter (Kruger and Krajewski, 2002) to ensure the accuracy of the measured DSDs in this study. Figure 2 shows the 2DVD-observed drop concentration with respect to the diameter and fall velocity during different seasons. The Brandes et al. (2002) relationship and the two ±60% limits are presented as solid and dashed black lines, respectively. Overall, the measured fall velocities of raindrops matched well with the empirically derived terminal fall speed, which suggests reliability of the 2DVD measurements. The filter removes 4.08%, 1.79%, 1.17%, and 1.55% of the total raindrops for summer, autumn, winter, and spring rainfall, respectively.

2.4. *Classification of rain types*

Based on the combination of 2DVD-observed rainfall intensity and MRR-observed vertical structure of radar reflectivity, three rain types, i.e., stratiform, convective, and shallow rain, are investigated. The method is the same as employed in Wen et al. (2016). Figure 3 presents an example of the measured vertical profile of reflectivity and the time series of the DSDs using the MRR and the 2DVD from 0000 to 1800 UTC 12 July 2014. The red, black, and purple bars at the top of Fig. 3a indicate the classified convective, stratiform, and shallow categories, respectively. Visible differences can be seen in the feature and DSD characteristics among the three rain types, indicating distinctions among the microphysical processes of different rain types (Wen et al., 2016). While stratiform rain contains a marked bright band, the top of shallow rain is too low to reach the melting layer, suggesting that the shallow precipitation forms directly in liquid form and no melting is present. As a result, the corresponding DSDs of shallow rain are composed mainly of high concentrations of small raindrops.

A total of 11 113, 5758, 3649, and 6545 1-min DSD samples are categorized by the classification scheme for the summer, autumn, winter, and spring rainfall, respectively. Note that the fraction of uncategorized samples is about 13.2% in terms of rainfall contribution for the whole dataset of 2DVD measurements. The 2DVD-measured frequencies of precipitation for different rain types during the four seasons are listed in Table 1. The convective rain contributes 77.52%, 42.98%, and 42.50% of the whole categorized rainfall amount for the precipitation during summer, autumn, and spring at the JN site. The winter rainfall is completely composed of stratiform rain (excluding snowfall).

3. Environmental backgrounds

Since the convective available potential energy (CAPE) and the amounts of moisture are two important factors usually used to determine the formation and growth of convection (Smith, 1997), the seasonal differences of these two parameters will be discussed below.

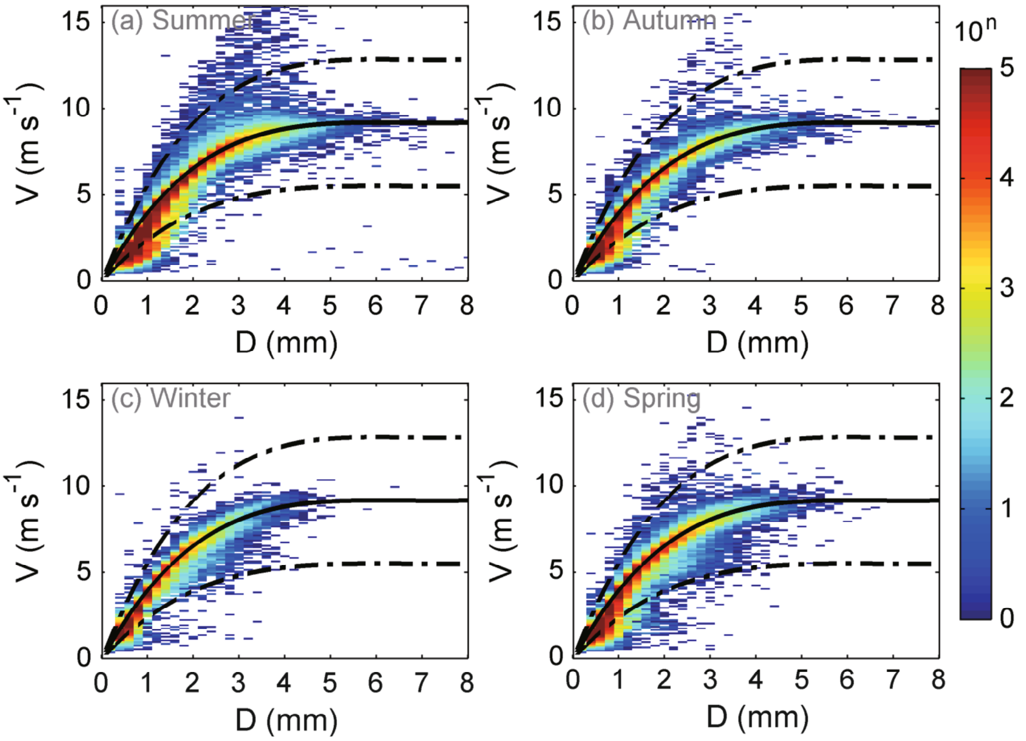

Fig. 2. Occurrence of velocity-diameter combinations with drop counts on a log scale from 2DVD observations for the four seasons. The color shading represents the measured drop counts. The black line indicates the Brandes et al. (2002) terminal drop velocity and the two dashed lines represent the ±60% filter of drops.

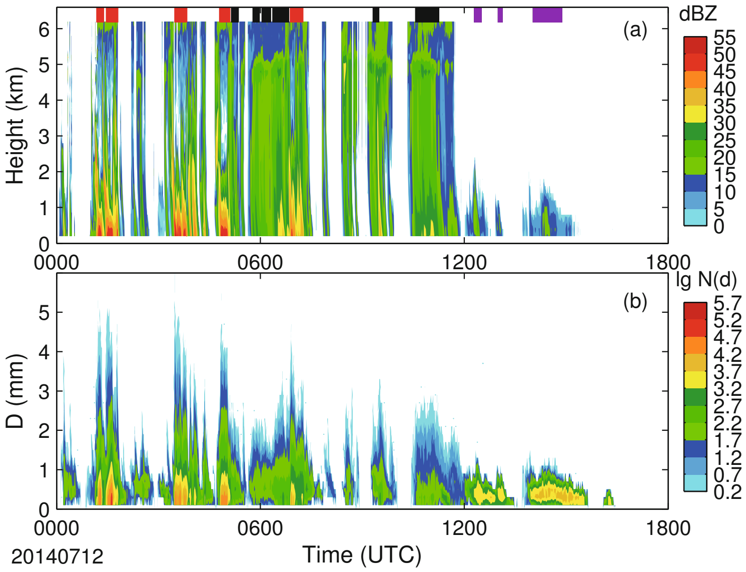

Fig. 3. (a) The MRR-measured vertical profile of reflectivity (color shading) from 0000 to 1800 UTC 12 July 2014. The classified convective, stratiform, and shallow samples are illustrated by red, black, and purple bars at the top of the diagram. (b) The 2DVD-measured time series of DSDs in logarithmic units of mm^{-1} m^{-3}.

Table 1. Integral rain parameters derived from the composite raindrop spectra for the three rain types during different seasons. Parameters N_t (m^{-3}), N_w (mm^{-1} m^{-3}), LWC (g m^{-3}), D_m (mm), σ_m (mm), and R (mm h^{-1}) are the total raindrop concentration, generalized raindrop concentration, liquid water content, mass-weighted mean diameter, the standard deviation of the mass spectrum with respect to D_m, and the rain rate, respectively.

Rain type	Season	Samples	D_m (mm)	N_t (m^{-3})	lgN_w (mm^{-1} m^{-3})	LWC (g m^{-3})	σ_m (mm)	R (mm h^{-1})
Convective	Summer	2701	1.41	8079	4.37	1.50	0.68	24.44
	Autumn	372	1.52	5505	4.12	1.08	0.76	18.87
	Winter	–	–	–	–	–	–	–
	Spring	571	1.40	6368	4.24	0.95	0.67	16.17
Stratiform	Summer	6882	1.16	627	3.78	0.15	0.44	2.35
	Autumn	4887	1.15	553	3.69	0.11	0.46	1.80
	Winter	3649	1.14	680	3.74	0.12	0.49	1.82
	Spring	4467	1.13	754	3.82	0.14	0.46	2.17
Shallow	Summer	1530	0.64	2763	4.97	0.21	0.19	1.95
	Autumn	499	0.60	3286	4.91	0.12	0.21	1.01
	Winter	–	–	–	–	–	–	–
	Spring	1507	0.74	2287	4.67	0.17	0.29	1.87
Total	Summer	11 113	1.15	1432	4.09	0.49	0.47	7.66
	Autumn	5758	1.13	748	3.82	0.18	0.46	2.84
	Winter	3649	1.14	680	3.74	0.12	0.49	1.82
	Spring	6545	1.06	1172	4.05	0.22	0.44	3.32

Figure 4 shows the seasonal mean of the reanalysis wind field and relative humidity at 850 hPa. As can be seen, the wind direction changes significantly from season to season at 850 hPa. The East Asian summer monsoon reaches its strongest period during summer, when adequate warm and moist air is transported from the Indian Ocean and South China Sea to the continent by the dominant southwesterly winds, resulting in the increasing of convective instability in this region. The mean 850 hPa relative humidity at the JN site is about 80% during this period. Under this circumstance, heavy rainfall events dominate the weather over South China and the middle of East China (Ding et al., 2010). During autumn, along with the weakening of the summer monsoon and invasion of the weak and cold air from the northwest, the prevailing winds become northerly to northeasterly in East China. The convection is generally weaker, with the mean relative humidity at 850 hPa decreasing to ~ 60% over the JN site.

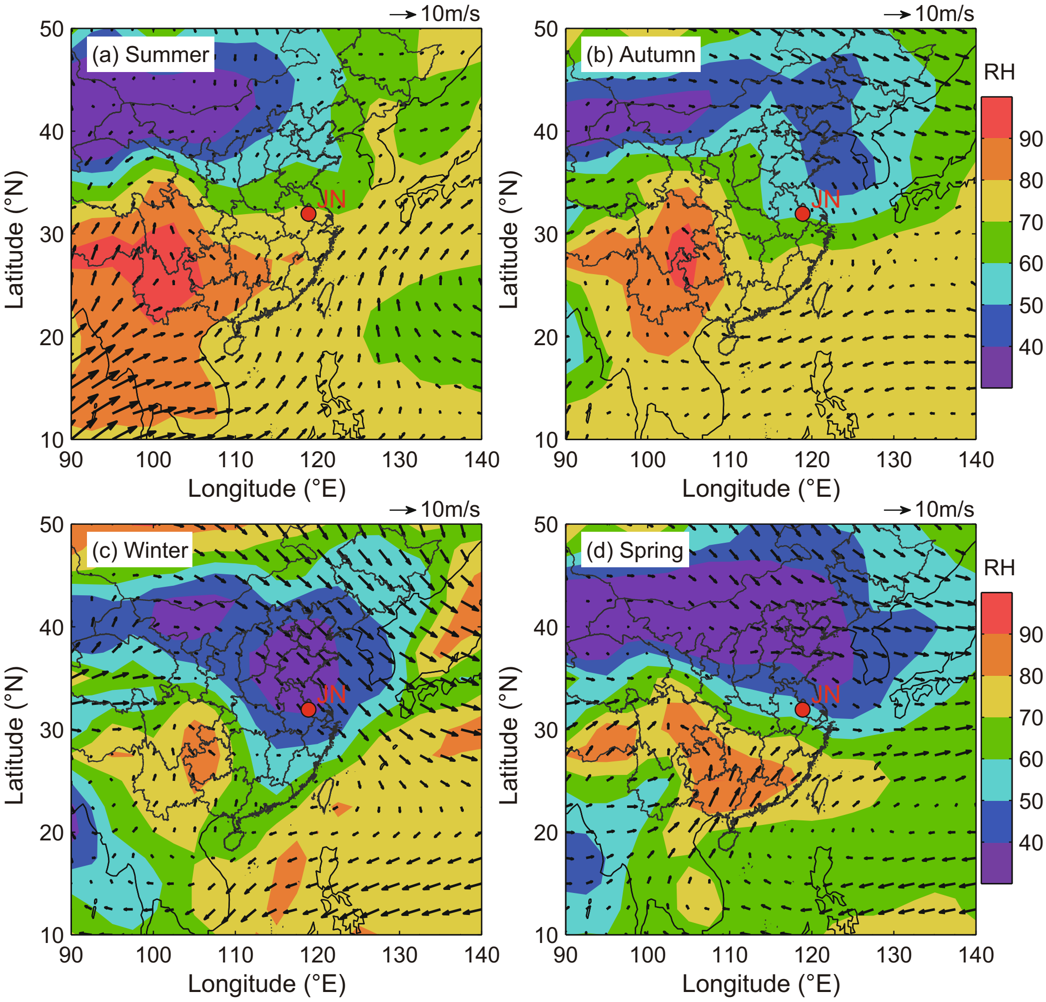

Fig. 4. Seasonal mean wind field and relative humidity (%) at 850 hPa based on the R2 data. The scale of the wind vector (10 m s^{-1}) is marked by wind arrows at the top of panels, while relative humidity is revealed by the color bar. JN = Jiangning site.

With the establishment of the East Asian winter monsoon, dry and cold air from the middle and high latitudes can reach as far as South and East China via the prevailing northwesterly winds. Under this circulation feature, the winter rainfall is relatively weak in East China, with a mean relative humidity at the JN site of around 40% during this season. The Asian summer monsoon is established again in mid-spring, and dominates the weather in South China. During this period, moderate moist air from the ocean is transported to East China, as the relative humidity significantly increases (~ 60%).

The CAPE calculated from in-situ sounding data at the JN site (twice a day) during different seasons is presented in Fig. 5. As can be seen, the CAPE during summer is the highest, with the mean value at ~ 958 J kg^{-1} and the maximum value reaching as high as 3100 J kg^{-1}, suggesting more intense rainfall during this period. Dramatic decreases occur during the other seasons. The mean CAPE value is about 155 J kg^{-1} and 230 J kg^{-1} during autumn and spring, respectively. Under the control of dry and cold air in winter, the CAPE

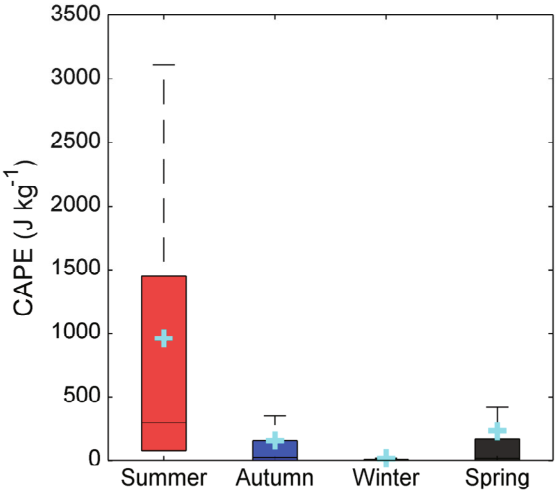

Fig. 5. CAPE value calculated from in-situ sounding data (twice a day) at the JN site for the four seasons, with plus signs represent the seasonal mean.

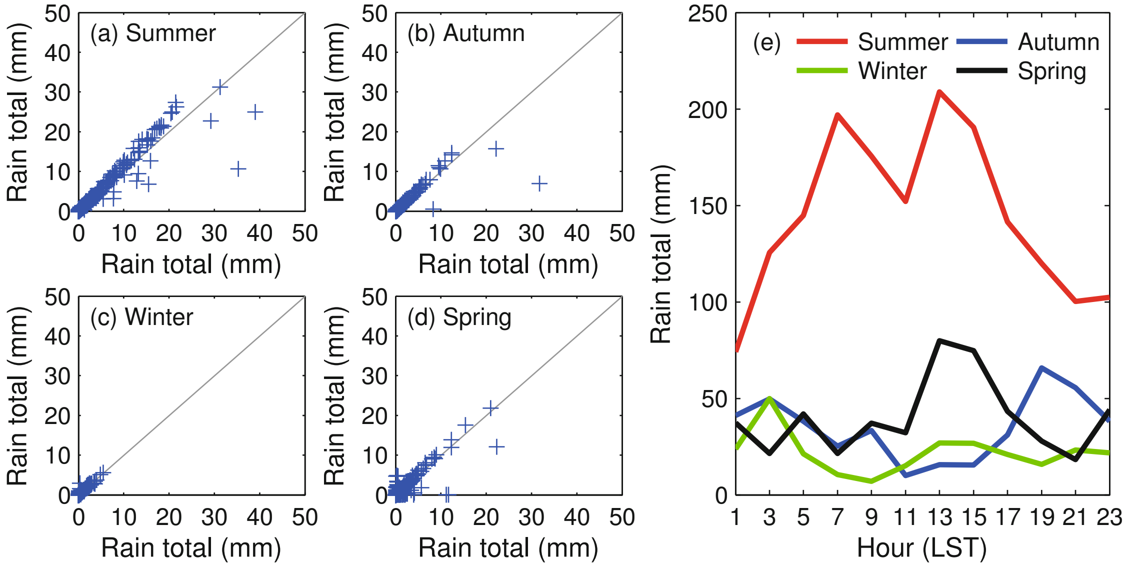

Fig. 6. (a–d) 2DVD (y-axis) versus rain gauge (x-axis) observed hourly rain total and (e) two-hourly accumulated total rainfall from 2DVD during different seasons.

value is negligible and convective rain is absent in East China.

4. Precipitation and DSD characteristics

While the differences in environmental background have been investigated above, more details about the precipitation under these circumstances and their related DSD characteristics will be discussed in the following text.

4.1. *Rainfall contribution*

Apart from some minor differences, the 2DVD-observed hourly rain shows good agreement with that of rain gauge measurements during all four seasons (Figs. 6a–d and Table 2), which again implies the reliability of 2DVD rainfall measurements. The two-hourly accumulated total rainfall for summer shows remarkably higher values than for the other seasons (Fig. 6e). The double peak of summer rainfall in East China inferred in previous studies (Yu et al., 2007a, b; Hsu et al., 2014) also shows up in the present study, with the morning peak at around 0600–1000 LST and the afternoon peak at around 1300–1500 LST. The spring rainfall only shows up with an afternoon peak, while that of autumn and winter occurs before and after midnight.

Table 2. The correlation coefficient (CC), standard deviation (SD, mm), percentage bias (Bias), and percentage absolute bias (ab. Bias) between 2DVD- and rain-gauge-observed hourly rain totals for the four seasons.

Season	CC	SD (mm)	Bias (%)	ab. Bias (%)
Summer	0.96	1.728	6.9	17.8
Autumn	0.839	1.537	−2.6	20.3
Winter	0.954	0.268	4.1	17.7
Spring	0.853	1.527	−1.2	36.1

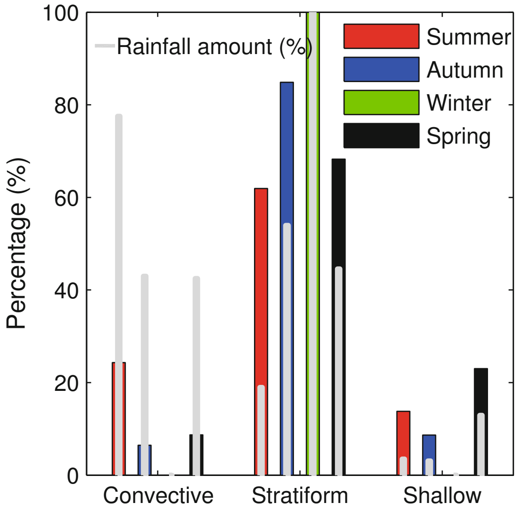

Fig. 7. Percentage occurrence and contribution to rainfall amount of different rain types during different seasons.

Figure 7 shows the percentage occurrence of different rain types and their contribution to rainfall amount during different seasons. There is a 24% chance that convective rain occurs in summer during the two-year period, which decreases abruptly to 6%–8% in autumn and spring, while that of stratiform rain increases from summer (62%) towards winter (100%) and then falls back in spring (68%). The occurrence of shallow rain is higher than convective rain in autumn and spring. When considering the contribution to rainfall amount, the summer rainfall is dominated by convective rain (77.5%). The contribution of stratiform rain to rainfall amount is equal to or even larger than that of convective rain during the other seasons. Shallow rain is negligible (~ 3%)

during most of the seasons, but still contributes as much as 13% to total rainfall in spring.

4.2. *Distribution of* D_m *and* N_w

The cumulative distribution functions (CDFs) of R, D_m and $\lg N_w$ with respect to population and rainfall contribution are presented in Fig. 8. In winter, the precipitation under 10 mm h^{-1} shows the highest population and contributes nearly 100% to rainfall amount. During spring and autumn, over 95% of precipitation is lower than 15 mm h^{-1}, contributing to 70%–75% of rainfall amount. On the contrary, the precipitation higher than 15 mm h^{-1} (which contains a population of ~ 14%) still contributes ~ 65% to rainfall amount in summer. The mean R is about 7.66, 2.84, 1.82 and 3.32 mm h^{-1} in summer, autumn, winter and spring, respectively.

Seasonal variations can also be seen in the CDFs of DSD parameters, i.e., D_m and $\lg N_w$ (Figs. 8b and c). The mean D_m value is about 1.15, 1.13, 1.14 and 1.06 mm from summer to spring, respectively. Nearly 75%–85% of precipitation is characterized by D_m values lower than 1.3 mm during the four seasons. Their contribution to rainfall amount, however, shows up with a vast range of values (from 70% in winter to 40% in summer). When D_m is larger than 1.5 mm, the rainfall contribution in autumn is the highest, suggesting a higher occurrence frequency of larger drops. The population curves of $\lg N_w$ is similar between autumn and winter (and between summer and spring), but the curves of rainfall contribution between them are distinctly different. For $\lg N_w$ lower than 4.0, the populations are similar (about 90%) in autumn and winter, but their contribution to rainfall amount is about 60% and 80%, respectively. Differences can also be seen between spring and summer; that is, nearly 60% (55%) of precipitation contributes over 45% (25%) to rainfall amount in spring (summer).

Overall, A relatively larger raindrop diameter and the highest concentration of raindrops during summer result in the highest mean R among the four seasons. On the contrary, winter rainfall is characterized by the lowest number concentration, and thus has the lowest mean R. Rainfall in spring is slightly higher than in autumn because it contains more raindrops, even though its mean raindrop diameter is the smallest among the four seasons.

To better reveal the differences of D_m and $\lg N_w$ for different rain types, Fig. 9 shows scatterplots of averaged D_m versus $\lg N_w$ for the three rain types during different seasons. One can see that the averaged D_m–$\lg N_w$ pair for the three rain types shows distinguishable differences during the four seasons, indicating significant differences in precipitation microphysics through different rainfall processes.

When considering different rain types during the four seasons, convective rain in autumn shows up with the largest D_m value but lowest $\lg N_w$ value (also see Table 1). In spring, the D_m value is slightly lower than in summer, and the $\lg N_w$ value is plotted roughly between summer and autumn. Over-

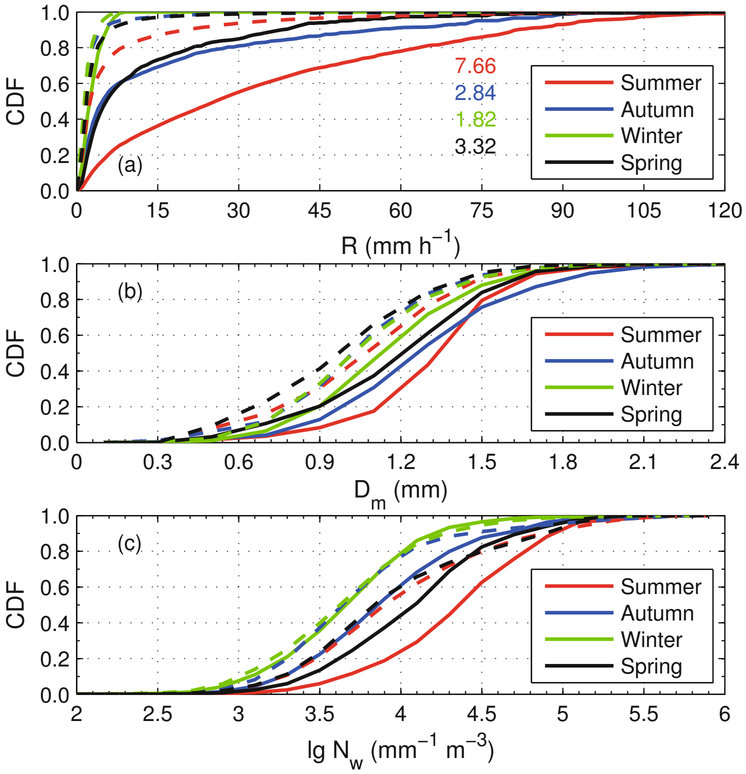

Fig. 8. CDF of population (dashed lines) and rainfall contribution (solid lines) of (a) R, (b) D_m, and (c) $\lg N_w$ during different seasons. The mean R of the four seasons is given in Fig. 8a as well, with corresponding colors.

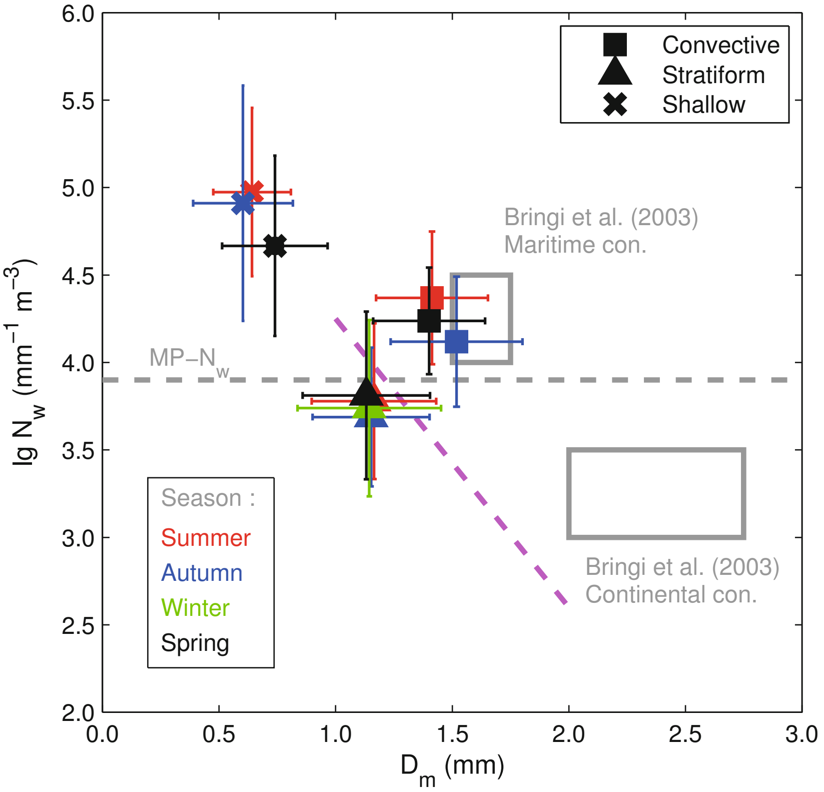

Fig. 9. Scatterplots of averaged D_m versus $\lg N_w$ for convective (squares), stratiform (triangles), and shallow (crosses) rain types during summer (red), autumn (blue), winter (green), and spring (black). The two gray rectangles correspond to the maritime and continental convective clusters, respectively, reported by Bringi et al. (2003). The pink dashed line is the stratiform line in Bringi et al. (2003). The gray dashed line is the Marshall-Palmer value of $\lg N_w$ (3.9) for exponential shape.

all, the mean D_m–$\lg N_w$ pairs of convective rain in East China are plotted roughly around the "maritime" cluster, as reported by Bringi et al. (2003), indicating a maritime nature of convective precipitation throughout the year in East China. Maritime convection is characterized by relatively higher concentrations of small drops than that of continental convection (Bringi et al., 2003).

When compared with that of convective rain, the averaged D_m–$\lg N_w$ pairs of stratiform rain show only slight differences among the four seasons, and they are all located left of the stratiform line in Bringi et al. (2003). Shallow rain generally has the lowest value of D_m but the highest value of $\lg N_w$, as compared with convective and stratiform rain. The averaged D_m–$\lg N_w$ pairs of shallow rain in summer and autumn are close to each other, while those of spring have higher values of D_m but lower values of $\lg N_w$, corresponding to the highest rainfall contribution by shallow rain ($\sim$13%) in spring. Moreover, the lowest D_m but relatively higher $\lg N_w$ for the whole categorized dataset in spring should also be attributed to the highest occurrence of shallow rain, as given in Fig. 7.

It is worth noting that the measured DSDs of the four seasons all show a lower value of D_m and a higher value of $\lg N_w$ compared to the 2DVD-measured mei-yu DSD in Okinawa, Japan (Bringi et al., 2006), and Taiwan (Chen, 2009), as well as the laser-optical Particle Size Velocity (PARSIVEL) disdrometer–measured mei-yu statistics in Nanjing (Chen et al., 2013). The differences in DSD characteristics among these studies are likely related to the different data samples, geographical locations, and instruments that were used. The topic, however, is beyond the scope of the present paper. More detailed comparative studies can be found in our previous work for summer (Wen et al., 2016) and typhoon (Wen et al., 2018) precipitation in East China, and the impacts of instrument limitations on estimated DSDs are given in Wen et al. (2017c).

4.3. *Composite raindrop spectra*

The composite raindrop spectra of the whole categorized dataset, and of the three rain types during different seasons, are presented in Fig. 10. Differences can be seen in the DSDs among different seasons and rain types.

For the total data (combination of convective, stratiform, and shallow rain), the summer spectrum has the largest maximum raindrop diameter (up to 6 mm) and highest number concentrations in all size bins (Fig. 10a), resulting in the highest LWC and R in summer. The spectrum for autumn contains

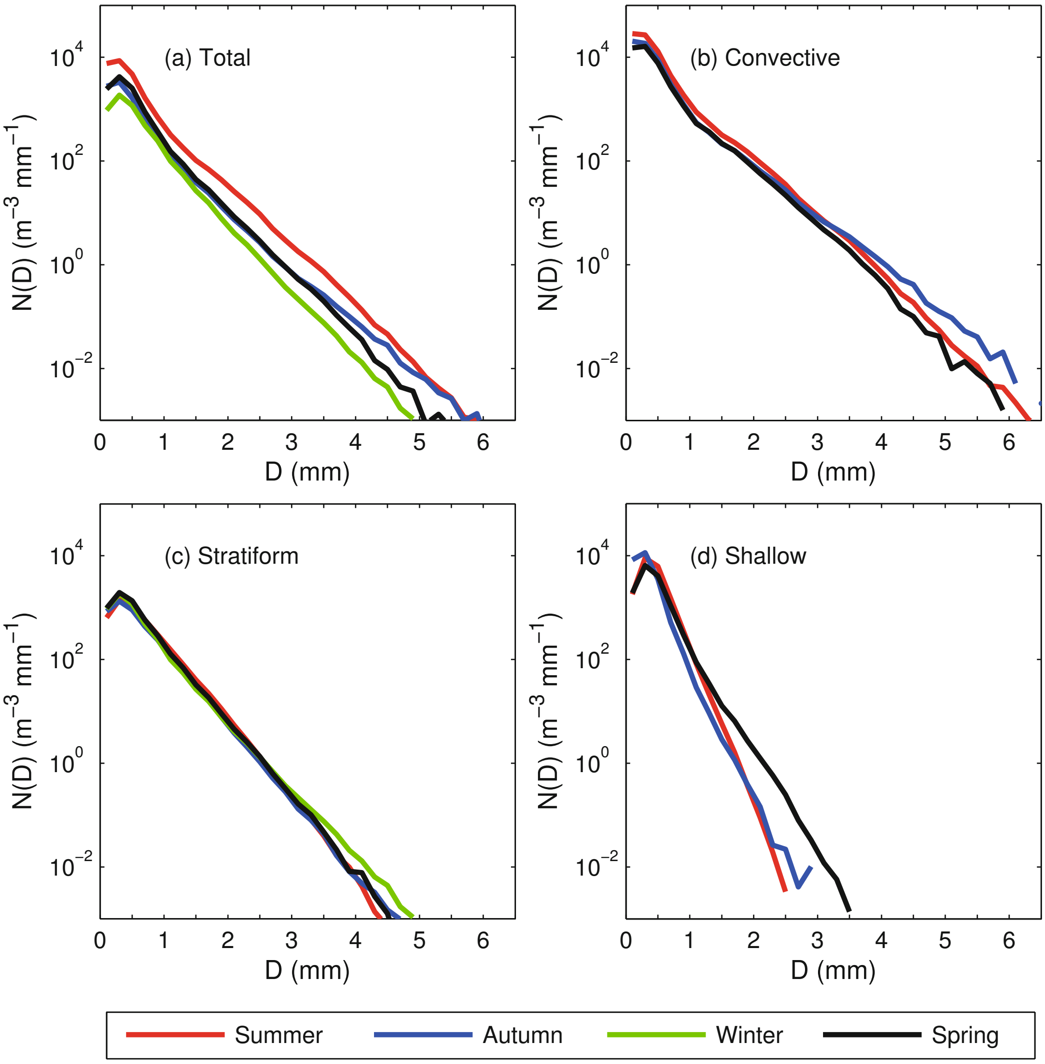

Fig. 10. Composite raindrop spectrum curves for different rain types during different seasons.

relatively lower (higher) number concentrations of raindrops at drop sizes smaller (larger) than 3.5 mm than those of spring because of the highest occurrence of shallow rain. Due to the absence of convective rain, the winter spectrum has the lowest number concentration and smallest maximum raindrop diameter (~ 4.9 mm), and consequently its mean LWC and R values are the lowest.

For convective rain, the autumn spectrum has the highest (a relatively lower) number concentration at drop sizes larger (smaller) than 3.5 mm (Fig. 10b). These features are likely attributable to a relatively dryer environment in autumn, which leads to the presence of fewer large drops through more sufficient raindrop collision–coalescence. Ultimately, autumn rainfall has the largest mean $D_{\rm m}$ but lowest mean $\lg N_{\rm w}$ value among the four seasons (see Table 1).

The stratiform spectra are narrower than those of convective rain (Figs. 10b and c). The four curves agree well with each other, except that the winter spectrum is characterized by slightly higher concentrations at drop sizes larger than 3 mm. The shallow spectra are the narrowest but they contain higher concentrations than those of stratiform spectra below 1 mm in diameter (Fig. 10d), resulting in higher LWC but lower $D_{\rm m}$ values. The shallow spectra of spring have higher concentrations above 1.2 mm in diameter, with the maximum raindrop diameter at about 3.5 mm. The differences in the composite raindrop spectra are likely attributable to the variation in environmental backgrounds for the different rain types and seasons, as well as the differences in microphysical and dynamic processes. While the environmental backgrounds have been discussed above, a more detailed investigation of the seasonal variations of microphysical/dynamic processes in precipitation is needed in future research.

4.4. *Derived relations*

The accuracy of rainfall kinetic energy (KE) measurement is crucial for the estimation of soil erosion, because the KE of raindrops will cause splashing of soil particles on the earth, which then leads to the initiation of soil erosion (Wang et al., 2014). In other words, more accurate measurements of rainfall KE and R would help with better estimating rainfall erosivity (Cevasco et al., 2015). The KE of a raindrop KE_0 is estimated based on raindrop size and fall velocity:

$$\mathrm{KE}_0 = \frac{1}{2}mv^2 = \frac{1}{12}\times 10^{-3}\pi\rho v^2 D^3 \ , \qquad (2)$$

where m, ρ, and v represent the mass (g), the density of water (1 g cm^{-3}), and the velocity (m s^{-1}), respectively. In this study, the 1-min KE is calculated from the 1-min DSD and drop velocity measurements by 2DVD using Eq. (3) as follows:

$$\mathrm{KE} = \frac{\sum_{i=1}^{n} N\mathrm{KE}_0}{aP_{\mathrm{r}}} = \frac{\sum_{i=1}^{n} \frac{1}{12}\times 10^{-3} N\pi\rho v_i^2 D_i^3}{aP_{\mathrm{r}}} \ , \qquad (3)$$

where n is the total number of bins (41 in this study), with N, a and P_{r} representing the number of raindrops in a size and velocity bin i, the sample area of 2DVD (0.01 m^2), and rainfall per minute (mm), respectively.

To better reveal the variability of KE with respect to R during different seasons, scatterplots of KE versus R and their fitted relationships using a least-squares method are shown in Fig. 11. The exponents of the KE–R relationships are all positive, suggesting that the KE values are enhanced with rainfall intensity. We suspect this is possibly due to the presence of more large drops with high terminal velocity during heavy rainfall. However, for $R > 60$ mm h^{-1}, the magnitude of KE enhancement decreases with rainfall intensity, and the KE values approach a stable value around 20–25 J m^{-2} mm^{-1}. Previous studies have reached a similar result, but with a different upper limit. For example, Carollo et al. (2016) proposed an upper limit at 40 mm h^{-1}, while that of Wischmeier and Smith (1978) was about 70 mm h^{-1}. This phenomenon (the upper limit of KE) corresponds to the equilibrium state of DSD, where the raindrops coalescence and breakup processes are reached near balance. Under this state, the raindrop size and fall velocity remain almost constant, and the increase in R mainly benefits from the increase in raindrop number concentration (Bringi and Chandrasekar, 2001; Wen et al., 2016).

The fitted KE–R relation for the whole categorized dataset is also given. It agrees well with that of summer and spring, but tends to underestimate the KE value for a given R in autumn and winter. Moreover, the dispersion between

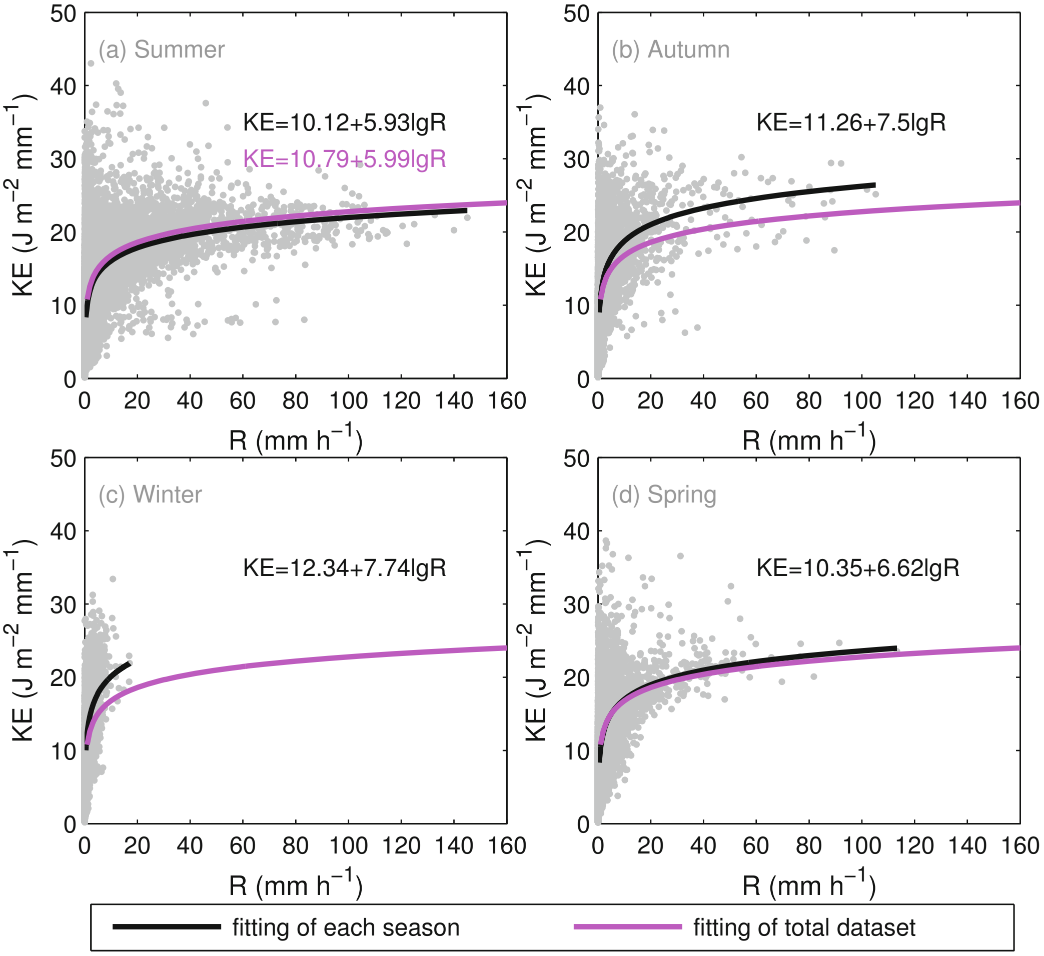

Fig. 11. Scatterplots of one-minute KE versus R for the four seasons. The fitted KE–R relationships using a least-squares method are provided in each panel (black lines). The magenta line represents the fitted KE–R relationship for the whole categorized dataset.

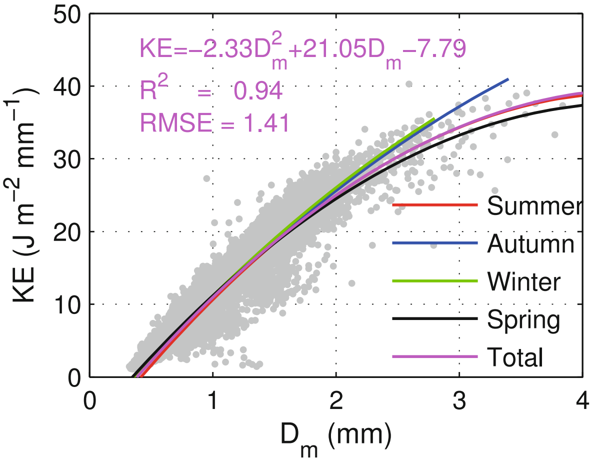

Fig. 12. Scatterplots of observed D_m versus KE for different seasons. The fitted power law relationships for the four seasons and the whole categorized dataset using a least-squares method are provided in corresponding colors.

the fitted curves and the measured values increases dramatically during weak rainfall ($R < 10$ mm h^{-1}). Hence, in this study, a new form of KE estimator based on DSD, i.e. the KE–D_m relationship, is firstly proposed using a polynomial least-squares fit, as shown in Fig. 12. One can see that the fitted KE–D_m relationships exhibit higher agreement with measured KE–D_m pairs at all ranges than that of the KE–R relationship, implying a good performance for rainfall KE estimation using the KE–D_m estimator. The four KE–D_m curves show good agreement with each other when D_m is under 2 mm, as with that of the whole dataset. The gaps among the curves increase with the increase in D_m when larger than 2 mm. However, the percentage of D_m data points exceeding 2 mm is negligible (0.69%, 0.53%, 0.16% and 0.47% for summer, autumn, winter and spring, respectively; also see Fig. 8). Therefore, the KE–D_m relationship for the whole categorized dataset is fitted (magenta line in Fig. 12) and given as:

$$\mathrm{KE} = -2.33D_m^2 + 21.05D_m - 7.79\,. \tag{4}$$

The coefficient of determination (R^2) and RMSE of the fitting is 0.94 and 1.41 J m^{-2} mm^{-1}, respectively, which is quite good to validate the precision of the KE estimates by using the KE–D_m relationship derived for the whole categorized dataset. We believe that the KE–D_m relationship would be applicable for improving Global Precipitation Measurement (GPM) and/or ground-based polarimetric radar rainfall KE retrieval.

Besides KE estimators, many previous studies have also reported that the shape and slope (μ–Λ) constrained relations of DSD show variability with geographical location and climatological regime (e.g., Zhang et al., 2001, 2003; Cao et al., 2008). In this study, the μ–Λ relations have been derived for the four seasons (solid lines in Fig. 13a) following the same data procedure as in Cao et al. (2008). The derived μ–Λ relation is applicable for Λ ranging from 0 to 20, because larger Λ values mostly result from measurement errors rather than rainfall microphysics (Zhang et al., 2003). Since the differences in the coefficients of the relationships for the four seasons in East China are minor, the μ–Λ relation for the whole categorized dataset is derived and given as:

$$\mu = -0.021\Lambda^2 + 0.988\Lambda - 2.669\,. \tag{5}$$

For comparison, the μ–Λ relations derived from 2DVD measurements of precipitation in Florida (Zhang et al., 2003), Oklahoma (Cao et al., 2008), and Beijing (Wen et al., 2017a), and PARSIVEL measurements of precipitation in Nanjing (Chen et al., 2013) and Beijing (Tang et al., 2014), are given by dashed lines in Fig. 13a with corresponding colors.

Interestingly, the abovementioned μ–Λ relations can be sorted into three groups:

Group 1: Relations in Chen et al. (2013) and Tang et al. (2014) are close to each other, and will have much higher μ values for a given Λ than the other relations. The general underestimation of small drops and overestimation of large drops by the PARSIVEL disdrometer (Tokay et al., 2013; Wen et al., 2017c) that both of them used is likely to be the main cause, which would modify the DSDs yielding higher μ values.

Group 2: Because the same instrument (2DVD) and filter threshold are applied, the relation in Wen et al. (2017a) matches more to Zhang et al. (2003). The μ values are smaller than those in group 1 due to the more accurate observation of small raindrops by 2DVD.

Group 3: By using the same sorting and averaging based on two parameters (SATP) data processing procedure for 2DVD measurements, our newly derived μ–Λ relation gives similar results to those in Cao et al. (2008). The SATP method was introduced to minimize the sampling errors of 2DVD observations (Cao et al., 2008). Benefiting from this, the statistical errors of DSDs are reduced and thus the two relations present the smallest μ values for the same Λ. The minor differences between our newly derived relation and that in Cao et al. (2008) are likely attributable to the natural variability of DSDs between Oklahoma and East China. Moreover, it can be concluded from the above analysis that the derived μ–Λ relations vary a lot across different types of measurement instruments and data processing procedures. Wen et al. (2017a) reached a similar conclusion.

Disdrometer measurements are often used to derive variety forms of rainfall estimators (e.g., the widely used Z–R relationship) for radar QPE purposes. Since the diversity of DSDs will result in different coefficients in the estimators (e.g., Chandrasekar et al., 2003; Tokay et al., 2008), Z–R relations for East China rainfall during different seasons are derived for the three rain types (see Table 3; figure not shown). Note that the Z–R relations for summer rainfall are the same as in Wen et al. (2016). The coefficient and power of the derived Z–R relations for the three rain types are typically different from each other during all the four seasons. The coefficient of the shallow rain Z–R relation is the lowest compared to convective and stratiform rain in each season. Since Z is

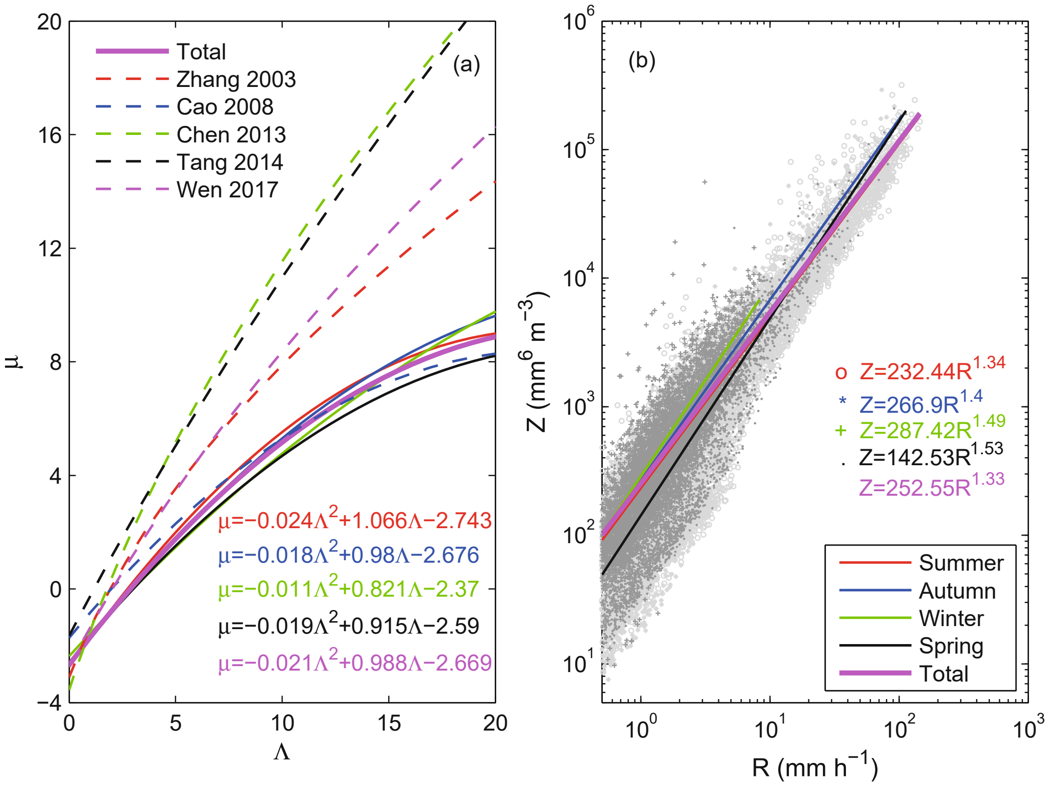

Fig. 13. (a) μ–Λ relations for the four seasons and the whole categorized dataset derived from 2DVD observations (solid lines and equations with corresponding colors). The dashed lines represent the derived relations by previous studies. (b) Scatterplots of Z–R values and the fitted power law relations for the four seasons without the separation of rain types derived from 2DVD observations.

Table 3. The coefficient (A) and power (b) of the Z–R relation ($Z = AR^b$) for the three rain types during different seasons.

Rain type	Season	A	b
Convective	Summer	230.85	1.34
	Autumn	261.57	1.41
	Winter	–	–
	Spring	125.87	1.56
Stratiform	Summer	193.73	1.54
	Autumn	229.85	1.56
	Winter	273.59	1.52
	Spring	243.65	1.41
Shallow	Summer	41.68	1.68
	Autumn	78.24	1.09
	Winter	–	–
	Spring	112.47	1.38
Total	Summer	232.44	1.34
	Autumn	266.9	1.4
	Winter	287.42	1.49
	Spring	142.53	1.53

more sensitive to D than to the raindrop concentration $N(D)$, for a given Z, the shallow rain (which contains higher concentrations of smaller drops than stratiform rain) would lead to a larger R.

The equations of fitted Z–R relations for the four seasons without the separation of rain types are further given with corresponding colors in Fig. 13b. One can see that the newly derived relationships for the four seasons are different from each other. While rainfall in winter seldom exceeds 10 mm h^{-1}, its $Z = 287.42R^{1.49}$ relationship has the highest coefficient and a relatively large exponent value, and the curve lies to the upper left of the other relationships. As concluded from Fig. 7 and Table 1, winter rainfall is entirely composed of stratiform rain, while that of other seasons contains not only stratiform but also shallow rain when $R < 10$ mm h^{-1}. Therefore, winter rainfall has the lowest R for a given Z due to the absence of shallow rain. As expected, rainfall in spring would have the largest R for a given Z because of the highest occurrence frequency of shallow rain, which leads to its $Z = 142.53R^{1.53}$ relationship having the lowest coefficient and largest exponent value.

For $R > 10$ mm h^{-1} (which is mostly categorized as convective rain), $Z = 266.9R^{1.4}$ for autumn rainfall would estimate the lowest R, followed by spring and summer rainfall, for a given Z. Because of the relatively small mean $D_{\rm m}$ and largest $N_{\rm t}$ in summer, the $Z = 232.44R^{1.34}$ relationship has the smallest exponent among the four relationships, suggesting the highest R estimation for the same Z value during convective (heavy) rainfall. The fitted $Z = 252.55R^{1.33}$ for the whole categorized dataset throughout the year fits the measured data well on the whole.

The above analyses suggest that the variability of DSDs is a major source of diversity in derived relations (i.e. KE–R, KE–D_m, μ–Λ, and Z–R relations) based on disdrometer measurements. As a result, the accuracy of localized remote estimation is limited and the practical applications of these estimators are impeded. In this study, using the currently most accurate 2DVD measurements, more accurate seasonal precipitation microphysics is investigated in East China. On this basis, the above-mentioned relations are derived for rainfall during the four seasons in this specific climatological region. Also, we believe that these relations will certainly with improving the accuracy of rainfall KE estimation, DSD retrieval, and QPE in this region.

5. Summary and conclusions

In this paper, the seasonal characteristics of rainfall microphysics in East China are investigated using data from the observations of a 2DVD and a vertically pointing MRR. The precipitation and raindrop size distribution characteristics are revealed for different rain types and seasons. The localized rainfall estimators based on disdrometer measurements are further derived. The main conclusions of this study can be summarized as follows:

(1) Benefiting from the strongest CAPE and the highest amounts of moisture, summer rainfall is dominated by convective rain (77.5%), while during the other seasons the contribution of stratiform rain to rainfall amount is equal to or even larger than that of convective rain. Winter rainfall is completely composed of stratiform rain. Shallow rain is negligible (~ 3%) during most seasons, but still contributes ~ 13% to total rainfall in spring.

(2) A relatively larger raindrop diameter and the highest concentration of raindrops during summer result in the highest mean R among the four seasons. On the contrary, winter rainfall is characterized by the lowest number concentration of raindrops, and thus has the lowest mean R. Overall, the mean D_m–lgN_w pairs of convective rain in East China are plotted roughly around the "maritime" cluster, as reported by Bringi et al. (2003), indicating a maritime nature of convective precipitation throughout the year in this specific region.

(3) The rainfall KE is enhanced (but the magnitude of enhancement decreases) with rainfall intensity, and it approaches a stable value of around 20–25 J m^{-2} mm^{-1} for $R > 60$ mm h^{-1}. Previous studies reached a similar result, but with a different upper limit (Wischmeier and Smith, 1978; Carollo et al., 2016). The fitted KE–D_m relationship for the whole dataset, with an R^2 and RMSE of the fitting of 0.94 and 1.41 J m^{-2} mm^{-1} respectively, imply a good performance of KE estimation by using the KE–D_m estimator. It would certainly help with improving the accuracy of GPM DPR and/or ground-based polarimetric radar rainfall KE retrieval.

(4) The differences in the coefficients of the derived μ–Λ relations for the four seasons are minor. The μ–Λ relation for the whole categorized dataset gives similar results to those in Cao et al. (2008) for Oklahoma rainfall, even though they have different coefficients. Derived μ–Λ relations vary across different types of measurement instruments and data processing procedures. Z–R relations derived for the four seasons show differences in the coefficient and exponent values.

Although some interesting findings have been obtained on the seasonal variations of DSD characteristics in East China, the results are still not well addressed due to the still limited data samples. The physical/microphysical processes resulting in the differences of seasonal precipitation microphysics are worthy of further study. The advanced GPM and/or polarimetric radar observations would be helpful, and we plan to conduct further research along these lines in the future.

Acknowledgements. This work was primarily supported by the National Key Research and Development Program of China (Grant No. 2017YFC1501703), the National Natural Science Foundation of China (Grant Nos. 41875053, 41475015 and 41322032), and the National Fundamental Research 973 Program of China (Grant Nos. 2013CB430101 and 2015CB452800). The observational data used in this study were collected by a National 973 Project (Grant No. 2013CB430101), and any requests for the data can be made at http://scw973.nju.edu.cn/ or by contacting the project office at yang.zhengwei@nju.edu.cn.

REFERENCES

Brandes, E. A., G. F. Zhang, and J. Vivekanandan, 2002: Experiments in rainfall estimation with a polarimetric radar in a subtropical environment. *J. Appl. Meteor.*, **41**, 674–685, https://doi.org/10.1175/1520-0450(2002)041<0674:EIREWA>2.0.CO;2.

Brandes, E. A., K. Ikeda, G. F. Zhang, M. Schönhuber, and R. M. Rasmussen, 2007: A statistical and physical description of hydrometeor distributions in Colorado snowstorms using a video disdrometer. *Journal of Applied Meteorology and Climatology*, **46**, 634–650, https://doi.org/10.1175/JAM2489.1.

Bringi, V. N., and V. Chandrasekar, 2001: *Polarimetric Doppler Weather Radar: Principles and Applications*. Cambridge University Press, Cambridge, U. K., 636 pp.

Bringi, V. N., V. Chandrasekar, J. Hubbert, E. Gorgucci, W. L. Randeu, and M. Schoenhuber, 2003: Raindrop size distribution in different climatic regimes from disdrometer and dual-polarized radar analysis. *J. Atmos. Sci.*, **60**, 354–365, https://doi.org/10.1175/1520-0469(2003)060<0354:RSDIDC>2.0.CO;2.

Bringi, V. N., M. Thurai, K. Nakagawa, G. J. Huang, T. Kobayashi, A. Adachi, H. Hanado, and S. Sekizawa, 2006: Rainfall estimation from C-band polarimetric radar in Okinawa, Japan: Comparisons with 2D-Video disdrometer and 400MHz wind profiler. *J. Meteor. Soc. Japan*, **84**, 705–724, https://doi.org/10.2151/jmsj.84.705.

Cao, Q., G. F. Zhang, E. Brandes, T. Schuur, A. Ryzhkov, and K. Ikeda, 2008: Analysis of video disdrometer and polarimetric radar data to characterize rain microphysics in Oklahoma. *Journal of Applied Meteorology and Climatology*, **47**, 2238–2255, https://doi.org/10.1175/2008JAMC1732.1.

Carollo, F. G., V. Ferro, and M. A. Serio, 2016: Estimating rainfall erosivity by aggregated drop size distributions. *Hydrological Processes*, **30**, 2119–2128, https://doi.org/10.1002/hyp.10776.

Cevasco, A., N. Diodato, P. Revellino, F. Fiorillo, G. Grelle, and F. M. Guadagno, 2015: Storminess and geo-hydrological events affecting small coastal basins in a terraced Mediterranean environment. *Science of the Total Environment*, **532**, 208–219, https://doi.org/10.1016/j.scitotenv.2015.06.017.

Chakravarty, K., and P. E. Raj, 2013: Raindrop size distributions and their association with characteristics of clouds and precipitation during monsoon and post-monsoon periods over a tropical Indian station. *Atmos. Res.*, **124**, 181–189, https://doi.org/10.1016/j.atmosres.2013.01.005.

Chakravarty, K., P. E. Raj, A. Bhattacharya, and A. Maitra, 2013: Microphysical characteristics of clouds and precipitation during pre-monsoon and monsoon period over a tropical Indian station. *Journal of Atmospheric and Solar-Terrestrial Physics*, **94**, 28–33, https://doi.org/10.1016/j.jastp.2012.12.016.

Chandrasekar, V., R. Meneghini, and I. Zawadzki, 2003: Global and local precipitation measurements by radar. *Radar and Atmospheric Science: A Collection of Essays in Honor of David Atlas*, R. M. Wakimoto, and R. Srivastava, Eds., Springer, 215–215, https://doi.org/10.1007/978-1-878220-36-3_9.

Chang, W.-Y., T.-C. C. Wang, and P.-L. Lin, 2009: Characteristics of the raindrop size distribution and drop shape relation in typhoon systems in the western Pacific from the 2D video disdrometer and NCU C-band polarimetric radar. *J. Atmos. Oceanic Technol.*, **26**, 1973–1993, https://doi.org/10.1175/2009JTECHA1236.1.

Chen, B. J., Y. Wang, and J. Ming, 2012: Microphysical characteristics of the raindrop size distribution in typhoon Morakot (2009). *Journal of Tropical Meteorology*, **18**, 162–171, https://doi.org/10.3969/j.issn.1006-8775.2012.02.006.

Chen, B. J., J. Yang, and J. P. Pu, 2013: Statistical characteristics of raindrop size distribution in the Meiyu Season observed in Eastern China. *J. Meteor. Soc. Japan*, **91**, 215–227, https://doi.org/10.2151/jmsj.2013-208.

Chen, B. J., J. Wang, and D. L. Gong, 2015: Raindrop size distribution in a midlatitude continental squall line measured by Thies optical disdrometers over East China. *Journal of Applied Meteorology and Climatology*, **55**, 621–634, https://doi.org/10.1175/JAMC-D-15-0127.1.

Chen, B. J., Z. Q. Hu, L. P. Liu, and G. F. Zhang, 2017a: Raindrop size distribution measurements at 4,500 m on the Tibetan Plateau during TIPEX-III. *J. Geophys. Res.*, **122**, 11 092–11 106, https://doi.org/10.1002/2017JD027233.

Chen, G., and Coauthors, 2017b: Improving polarimetric C-Band radar rainfall estimation with two-dimensional video disdrometer observations in Eastern China. *Journal of Hydrometeorology*, **18**, 1375–1391, https://doi.org/10.1175/JHM-D-16-0215.1.

Chen, Y. R., 2009: The characteristic of drop size distribution during SoWMEX. M.S. thesis, Institute of Atmospheric Physics, NCU, 68 pp. (in Chinese)

Das, S., and D. Ghosh, 2016: Dependency of rain integral parameters on specific rain drop sizes and its seasonal behaviour. *Journal of Atmospheric and Solar-Terrestrial Physics*, **149**, 15–20, https://doi.org/10.1016/j.jastp.2016.09.003.

Das, S., and A. Maitra, 2018: Characterization of tropical precipitation using drop size distribution and rain rate-radar reflectivity relation. *Theor. Appl. Climatol.*, **132**, 275–286, https://doi.org/10.1007/s00704-017-2073-1.

Das, S. K., M. Konwar, K. Chakravarty, and S. M. Deshpande, 2017: Raindrop size distribution of different cloud types over the Western Ghats using simultaneous measurements from Micro-Rain Radar and disdrometer. *Atmos. Res.*, **186**, 72–82, https://doi.org/10.1016/j.atmosres.2016.11.003.

Ding, Y. H., and J. C. L. Chan, 2005: The East Asian summer monsoon: An overview. *Meteor. Atmos. Phys.*, **89**, 117–142, https://doi.org/10.1007/s00703-005-0125-z.

Ding, Y. H., Y. J. Liu, Y. Sun, and Y. F. Song, 2010: Weakening of the Asian summer monsoon and its impact on the precipitation pattern in China. *International Journal of Water Resources Development*, **26**, 423–439, https://doi.org/10.1080/07900627.2010.492607.

Hsu, H.-H., T. J. Zhou, and J. Matsumoto, 2014: East Asian, Indochina and Western North Pacific Summer Monsoon-An update. *Asia-Pacific Journal of Atmospheric Sciences*, **50**, 45–68, https://doi.org/10.1007/s13143-014-0027-4.

Janapati, J., B. K. Seela, M. V. Reddy, K. K. Reddy, P. L. Lin, T. N. Rao, and C. Y. Liu, 2017: A study on raindrop size distribution variability in before and after landfall precipitations of tropical cyclones observed over southern India. *Journal of Atmospheric and Solar-Terrestrial Physics*, **159**, 23–40, https://doi.org/10.1016/j.jastp.2017.04.011.

Jayalakshmi, J., and K. K. Reddy, 2014: Raindrop size distributions of south west and north east monsoon heavy precipitations observed over Kadapa (14°4′N, 78°82′E), a semiarid region of India. *Current Science*, **107**, 1312–1320.

Jung, S.-A., D.-I. Lee, B. J.-D. Jou, and H. Uyeda, 2012: Microphysical Properties of Maritime Squall Line Observed on June 2, 2008 in Taiwan. *J. Meteor. Soc. Japan*, **90**, 833–850, https://doi.org/10.2151/jmsj.2012-516.

Kanamitsu, M., and Coauthors, 2002: NCEP dynamical seasonal forecast system 2000. *Bull. Amer. Meteor. Soc.*, **83**, 1019–1038, https://doi.org/10.1175/1520-0477(2002)083<1019:NDSFS>2.3.CO;2.

Kozu, T., K. K. Reddy, S. Mori, M. Thurai, J. T. Ong, D. N. Rao, and T. Shimomai, 2006: Seasonal and diurnal variations of raindrop size distribution in asian monsoon region. *J. Meteor. Soc. Japan*, **84A**, 195–209.

Kozu, T., T. Shimomai, Z. Akramin, Marzuki, Y. Shibagaki, and H. Hashiguchi, 2005: Intraseasonal variation of raindrop size distribution at Koto Tabang, West Sumatra, Indonesia. *Geophys. Res. Lett.*, **32**, L07803, https://doi.org/10.1029/2004GL022340.

Krajewski, W. F., and Coauthors, 2006: DEVEX-disdrometer evaluation experiment: Basic results and implications for hydrologic studies. *Advances in Water Resources*, **29**, 311–325, https://doi.org/10.1016/j.advwatres.2005.03.018.

Krishna, U. V. M., K. K. Reddy, B. K. Seela, R. Shirooka, P. L. Lin, and C. J. Pan, 2016: Raindrop size distribution of easterly and westerly monsoon precipitation observed over Palau islands in the Western Pacific Ocean. *Atmos. Res.*, **174–175**, 41–51, https://doi.org/10.1016/j.atmosres.2016.01.013.

Kruger, A., and W. F. Krajewski, 2002: Two-dimensional video disdrometer: A description. *J. Atmos. Oceanic Technol.*, **19**, 602–617, https://doi.org/10.1175/1520-0426(2002)019<0602:TDVDAD>2.0.CO;2.

Kumar, L. S., Y. H. Lee, J. X. Yeo, and J. T. Ong, 2011: Tropical rain classification and estimation of rain from Z-R (reflectivity-rain rate) relationships. *Progress in Electromagnetics Research*, **32**, 107–127, https://doi.org/10.2528/PIERB11040402.

Kumar, S. B., and K. K. Reddy, 2013: Rain drop size distribution characteristics of cyclonic and north east monsoon thunderstorm precipitating clouds observed over Kadapa (14.47°N, 78.82°E), tropical semi-arid region of India. *Mausam*, **64**, 35–48.

Liao, L., R. Meneghini, and A. Tokay, 2014: Uncertainties of GPM DPR rain estimates caused by DSD parameterizations. *Journal of Applied Meteorology and Climatology*, **53**, 2524–2537, https://doi.org/10.1175/JAMC-D-14-0003.1.

Maki, M., T. D. Keenan, Y. Sasaki, and K. Nakamura, 2001: Characteristics of the raindrop size distribution in tropical continental squall lines observed in Darwin, Australia. *J. Appl. Meteor.*, **40**, 1393–1412, https://doi.org/10.1175/1520-0450(2001)040<1393:COTRSD>2.0.CO;2.

Meshesha, D. T., A. Tsunekawa, M. Tsubo, N. Haregeweyn, and E. Adgo, 2014: Drop size distribution and kinetic energy load of rainfall events in the highlands of the Central Rift Valley, Ethiopia. *Hydrological Sciences Journal*, **59**, 2203–2215, https://doi.org/10.1080/02626667.2013.865030.

Niu, S. J., X. C. Jia, J. R. Sang, X. L. Liu, C. S. Lu, and Y. G. Liu, 2010: Distributions of raindrop sizes and fall velocities in a semiarid plateau climate: Convective versus stratiform rains. *Journal of Applied Meteorology and Climatology*, **49**, 632–645, https://doi.org/10.1175/2009JAMC2208.1.

Oue, M., T. Ohigashi, K. Tsuboki, and E. Nakakita, 2015: Vertical distribution of precipitation particles in Baiu Frontal Stratiform intense rainfall around Okinawa Island, Japan. *J. Geophys. Res.*, **120**, 5622–5637, https://doi.org/10.1002/2014JD022712.

Peters, G., B. Fischer, and T. Andersson, 2002: Rain observations with a vertically looking Micro Rain Radar (MRR). *Boreal Environment Research*, **7**, 353–362.

Radhakrishna, B., T. N. Rao, D. N. Rao, N. P. Rao, K. Nakamura, and A. K. Sharma, 2009: Spatial and seasonal variability of raindrop size distributions in southeast India. *J. Geophys. Res.*, **114**, D04203, https://doi.org/10.1029/2008JD011226.

Rao, T. N., B. Radhakrishna, K. Nakamura, and N. P. Rao, 2009: Differences in raindrop size distribution from southwest monsoon to northeast monsoon at Gadanki. *Quart. J. Roy. Meteor. Soc.*, **135**, 1630–1637, https://doi.org/10.1002/qj.432.

Rosenfeld, D., and C. W. Ulbrich, 2003: Cloud microphysical properties, processes, and rainfall estimation opportunities. *Radar and Atmospheric Science: A Collection of Essays in Honor of David Atlas*, R. M. Wakimoto, and R. Srivastava, Eds., American Meteorological Society, 237–258, https://doi.org/10.1007/978-1-878220-36-3_10.

Salles, C., J. Poesen, and D. Sempere-Torres, 2002: Kinetic energy of rain and its functional relationship with intensity. *J. Hydrol.*, **257**, 256–270, https://doi.org/10.1016/S0022-1694(01)00555-8.

Seela, B. K., J. Janapati, P. L. Lin, K. K. Reddy, R. Shirooka, and P. K. Wang, 2017: A comparison study of summer season raindrop size distribution between Palau and Taiwan, two islands in western Pacific. *J. Geophys. Res.*, **122**, 11 787–11 805, https://doi.org/10.1002/2017JD026816.

Shusse, Y., N. Takahashi, K. Nakagawa, S. Satoh, and T. Iguchi, 2011: Polarimetric radar observation of the melting layer in a convective rainfall system during the rainy season over the East China Sea. *Journal of Applied Meteorology and Climatology*, **50**, 354–367, https://doi.org/10.1175/2010JAMC2469.1.

Smith, R. K., 1997: *The Physics and Parameterization of Moist Atmospheric Convection*. Springer, 2176 pp, https://doi.org/10.1007/978-94-015-8828-7.

Tang, Q., H. Xiao, C. W. Guo, and L. Feng, 2014: Characteristics of the raindrop size distributions and their retrieved polarimetric radar parameters in northern and southern China. *Atmos. Res.*, **135–136**, 59–75, https://doi.org/10.1016/j.atmosres.2013.08.003.

Timothy, K. I., J. T. Ong, and E. B. L. Choo, 2002: Raindrop size distribution using method of moments for terrestrial and satellite communication applications in Singapore. *IEEE Trans. Antennas Propag.*, **50**, 1420–1424, https://doi.org/10.1109/TAP.2002.802091.

Tokay, A., and D. A. Short, 1996: Evidence from tropical raindrop spectra of the origin of rain from stratiform versus convective clouds. *J. Appl. Meteor.*, **35**, 355–371, https://doi.org/10.1175/1520-0450(1996)035<0355:EFTRSO>2.0.CO;2.

Tokay, A., P. G. Bashor, E. Habib, and T. Kasparis, 2008: Raindrop size distribution measurements in tropical cyclones. *Mon. Wea. Rev.*, **136**, 1669–1685, https://doi.org/10.1175/2007MWR2122.1.

Tokay, A., W. A. Petersen, P. Gatlin, and M. Wingo, 2013: Comparison of raindrop size distribution measurements by collocated disdrometers. *J. Atmos. Oceanic Technol.*, **30**, 1672–1690, https://doi.org/10.1175/JTECH-D-12-00163.1.

Ulbrich, C. W., 1983: Natural variations in the analytical form of the raindrop size distribution. *J. Appl. Meteor.*, **22**, 1764–1775, https://doi.org/10.1175/1520-0450(1983)022<1764:NVITAF>2.0.CO;2.

Ulbrich, C. W., and D. Atlas, 2007: Microphysics of raindrop size spectra: Tropical continental and maritime storms. *Journal of Applied Meteorology and Climatology*, **46**, 1777–1791, https://doi.org/10.1175/2007JAMC1649.1.

Ushiyama, T., K. Krishna Reddy, H. Kubota, K. Yasunaga, and R. Shirooka, 2009: Diurnal to interannual variation in the raindrop size distribution over Palau in the western tropical Pacific. *Geophys. Res. Lett.*, **36**, L02810, https://doi.org/10.1029/2008GL036242.

Vivekanandan, J., G. F. Zhang, and E. Brandes, 2004: Polarimetric radar estimators based on a constrained gamma drop size distribution model. *J. Appl. Meteor.*, **43**, 217–230, https://doi.org/10.1175/1520-0450(2004)043<0217:PREBOA>2.0.CO;2.

Wang, L., Z. H. Shi, J. Wang, N. F. Fang, G. L. Wu, and H. Y. Zhang, 2014: Rainfall kinetic energy controlling erosion processes and sediment sorting on steep hillslopes: A case study of clay loam soil from the Loess Plateau, China. *J. Hydrol.*, **512**, 168–176, https://doi.org/10.1016/j.jhydrol.2014.02.066.

Wang, M. J., K. Zhao, M. Xue, G. F. Zhang, S. Liu, L. Wen, and G. Chen, 2016: Precipitation microphysics characteristics of a Typhoon Matmo (2014) rainband after landfall over Eastern China based on polarimetric radar observations. *J. Geophys. Res.*, **121**, 12 415–12 433, https://doi.org/10.1002/2016JD025307.

Wen, G., H. Xiao, H. L. Yang, Y. H. Bi, and W. J. Xu, 2017a: Characteristics of summer and winter precipitation over northern China. *Atmos. Res.*, **197**, 390–406, https://doi.org/10.1016/j.atmosres.2017.07.023.

Wen, J., and Coauthors, 2017b: Evolution of microphysical structure of a subtropical squall line observed by a polarimetric radar and a disdrometer during OPACC in Eastern China. *J. Geophys. Res.*, **122**, 8033–8050, https://doi.org/10.1002/2016JD026346.

Wen, L., S. Liu, K. Zhao, Y. Li, and L. Li, 2015: Precision evaluation of micro rain radar observation in two precipitation events. *Meteorological Monthly*, **41**, 577–587, https://doi.org/10.7519/j.issn.1000-0526.2015.05.006. (in Chinese)

Wen, L., K. Zhao, G. F. Zhang, M. Xue, B. W. Zhou, S. Liu, and X. C. Chen, 2016: Statistical characteristics of raindrop size distributions observed in East China during the Asian summer monsoon season using 2-D video disdrometer and micro rain radar data. *J. Geophys. Res*., **121**, 2265–2282, https://doi.org/10.1002/2015JD024160.

Wen, L., K. Zhao, G. F. Zhang, S. Liu, and G. Chen, 2017c: Impacts of instrument limitations on estimated raindrop size distribution, radar parameters, and model microphysics during Mei-Yu Season in East China. *J. Atmos. Oceanic Technol*., **34**, 1021–1037, https://doi.org/10.1175/JTECH-D-16-0225.1.

Wen, L., and Coauthors, 2018: Drop size distribution characteristics of Seven Typhoons in China. *J. Geophys. Res*., **123**, 6529–6548, https://doi.org/10.1029/2017JD027950.

Wischmeier, W. H., and D. D. Smith, 1978: *Predicting Rainfall Erosion Losses: A Guide to Conservation Planning*. *US Department of Agriculture*, 58 pp.

Xue, M., 2016: Preface to the special issue on the “Observation, Prediction and Analysis of severe Convection of China” (OPACC) national “973” project. *Adv. in Atmos. Sci*., **33**(10), 1099–1101, https://doi.org/10.1007/s00376-016-0002-3.

Yu, R. C., Y. P. Xu, T. J. Zhou, and J. Li, 2007a: Relation between rainfall duration and diurnal variation in the warm season precipitation over central eastern China. *Geophys. Res. Lett*., **34**, L13703, https://doi.org/10.1029/2007GL030315.

Yu, R. C., T. J. Zhou, A. Y. Xiong, Y. J. Zhu, and J. M. Li, 2007b: Diurnal variations of summer precipitation over contiguous China. *Geophys. Res. Lett*., **34**, L01704, https://doi.org/10.1029/2006GL028129.

Zawadzki, I., and M. De Agostinho Antonio, 1988: Equilibrium raindrop size distributions in tropical rain. *J. Atmos. Sci*., **45**, 3452–3459, https://doi.org/10.1175/1520-0469(1988)045<3452:ERSDIT>2.0.CO;2.

Zhang, G. F., J. Vivekanandan, and E. Brandes, 2001: A method for estimating rain rate and drop size distribution from polarimetric radar measurements. *IEEE Trans. Geosci. Remote Sens*., **39**, 830–841, https://doi.org/10.1109/36.917906.

Zhang, G. F., J. Vivekanandan, E. A. Brandes, R. Meneghini, and T. Kozu, 2003: The shape-slope relation in observed gamma raindrop size distributions: Statistical error or useful information? *J. Atmos. Oceanic Technol*., **20**, 1106–1119, https://doi.org/10.1175/1520-0426(2003)020<1106:TSRIOG>2.0.CO;2.

Zhang, G. F., J. Z. Sun, and E. A. Brandes, 2006: Improving parameterization of rain microphysics with disdrometer and radar observations. *J. Atmos. Sci*., **63**, 1273–1290, https://doi.org/10.1175/JAS3680.1.